Microwave Engineering
Ulm University

ulm university universität
uulm

Coherent Multistatic MIMO Radar Networks Based on Repeater Tags

Benedikt Meinecke, Maximilian Steiner, Johannes Schlichenmaier, Jürgen Hasch, and Christian Waldschmidt

DOI: 10.1109/TMTT.2019.2916796

Coherent Multistatic MIMO Radar Networks Based on Repeater-Tags

Benedikt Meinecke, Maximilian Steiner, *Student Member, IEEE*, Johannes Schlichenmaier, *Student Member, IEEE,* Jürgen Hasch, *Senior Member, IEEE* and Christian Waldschmidt, *Senior Member, IEEE*

***Abstract*—In this paper, a coherent multistatic radar network with a novel system architecture is presented, which circumvents the general problems of clock distribution and phase noise related signal-to-noise ratio (SNR) issues. The proposed network consists of a variable number of multiple-input multiple-output (MIMO) radar sensors and a variable number of repeater tags, all of which operate incoherently on the hardware level. In a minimum configuration, the network only consists of one MIMO radar sensor and a repeater tag. The theory behind such a multistatic network is mathematically derived and simulations are presented to show key aspects of the network, i.e. multistatic range and Doppler measurements as well as high resolution angle estimation exploiting a very large virtual aperture spanning the whole network. Measurements with one sensor and one repeater tag at 77 GHz are carried out to verify the simulations. The measurements show that the bistatic path between the sensor and repeater tag retains coherency.**

***Index Terms*—Bistatic, coherency, compressed sensing, direction-of-arrival (DOA) estimation, multiple-input multiple-output (MIMO) radar, networks, radar transceivers, radar systems, sensor, repeater**

I. Introduction

In microwave engineering, mm-wave radar sensors are used to enable a wide range of technical applications [1]. These sensors are becoming increasingly more capable, more integrated and are operating at higher frequency bands. With multiple-input multiple-output (MIMO) and multiplexing approaches, e.g. time division multiplexing [2], sensor properties like the total aperture can be further improved. Sparse antenna arrays reduce the required number of antenna elements for a given aperture size [3]. Novel two-dimensional antenna structures also pose a viable way to improve sensor performance [4]. To attain even higher performance, single sensors can be used as building blocks of larger structures, namely sensor networks. Such networks consist of multiple distributed sensor nodes, providing substantially more information. In addition to the monostatic response, the network can provide multistatic information about range, velocity, angle, and radar cross section of targets in the scene. The ability to utilize the highly desirable multistatic information of the radar sensor network depends upon the coupling between the nodes, which can be linked incoherently or coherently. In case of a coherent operation, the reference clock is commonly derived to enable joint processing. An illumination of targets from different aspect angles can lead to a more robust target detection, as the power reflected from the targets changes as a function of the incidence angle of the radar wavefront. Sensor networks without a reference clock have been realized using commonly triggered single sensors ([5], [6]) or by making use of multilateration [7]. Coherent bistatic links of multiple sensors that were not coherently coupled on a hardware level have also been investigated previously [8]. The problem that these networks face is the generation of coherency. If multiple sensors are not coupled coherently, but triggered at the same instant to produce the same transmit signal, the bistatic responses will have signal coherency or at least this coherency can be generated by appropriate signal processing as shown in [9]. This is essential but not sufficient to make use of the bistatic path because the noise coherency is of equal importance, as was shown in [9]. The monostatic measurement of typical radar sensors benefits from a single local oscillator (LO) being used to generate the transmit signal, as well as for the down-conversion of the received reflection. Hence, the phase noise of the received signal correlates with the phase noise of the transmitter, and therefore greatly suppresses the phase noise because of the range correlation effect [10]. This does not happen for the bistatic path in a non-coherent network, as the two involved sensor nodes will differ in their phase noise and, therefore, degrade the signal-to-noise ratio. A possible solution to work around the phase noise problem is the distribution of the transmit signal to each respective sensor node, so that the LO signal of the mixer in the receive path is always the same. This is often not feasible, as a transmission line or a waveguide between the nodes is too costly or cumbersome.

In this paper, a new approach is evaluated, which circumvents the phase noise problem and, therefore, enables the evaluation of the bistatic path without a wired coupling of the nodes. This is achieved by introducing a transceiver element (in the following called "repeater tag" or "tag") to the multistatic network. The tag has the ability to amplify frequency-modulated-continuous-wave (FMCW) signals at — in our case — 77 GHz as well as shifting them slightly in frequency by a built-in binary-phase-shift-keying (BPSK) modulator. A signal radiated from a sensor in the network is received by this repeater tag bistatically via the target. The signal is transmitted back over the bistatic path and is received and processed in the sensor node that initially radiated into the direction of the target. Since the path loss via the bistatic path

B. Meinecke, M. Steiner, J. Schlichenmaier and C. Waldschmidt are with the Institute of Microwave Engineering, Ulm University, 89081 Ulm, Germany (e-mail: benedikt.meinecke@uni-ulm.de)

J. Hasch is with the Corporate Sector Research and Advance Engineering of Robert Bosch GmbH, 70465 Stuttgart, Germany

The authors would like to thank the German Federal Ministry of Education and Research (BMBF) in the framework of the KoRRund project (Grant 16ES0580) for funding this work.

affects the power level with the fourth root of the distance for point targets, the tag needs to amplify the bistatically received signal. This ensures that the signal can be sent out again with enough transmit power to be able to cover the bistatic path a second time. This bistatic signal coming from the repeater tag is mixed with the original receive signal and will not suffer the problem of missing phase noise coherency mentioned earlier. Although the phase noise is higher for the bistatic path than for the monostatic one because of the increased distance, the phase noise is still not limiting the systems detection performance [11]. To be able to discern the bistatic from the monostatic signal at the sensor, the tag shifts the frequency of the signal by a small frequency step. This frequency step is so small, that its phase noise contribution is negligible, as the phase noise contribution of the sensor is orders of magnitude higher. The frequency multiplication within the sensor worsens the phase noise by the squared frequency multiplication factor [12]. The tag does not suffer from this degradation, as no frequency multiplication is applied.

The paper is organized as follows: In Section II, the concept and system architecture of the radar network with repeater tags are presented. Based on this, a signal model for the network is derived in Section III. Here the known chirp sequence modulation is extended to include the repeater tag. In Section IV the complete network with the joint processing of sensor and tags is described. Afterwards, simulations of the complete system are conducted in Section V. Finally, the simulations are validated by measurements with one sensor and one tag in Section VI.

II. Concept and System Architecture

In this section the system and network concept with transceiver tags are introduced. Starting from a MIMO configuration with one sensor ([14], [15]), the network is built by adding one or more tag nodes. A schematic drawing of such a configuration is shown in Fig. 1. Also, the general structure of the repeater tag is shown there. A front side view of the tag is provided in Fig. 2. An extensive description of the tag hardware with all system parameters can be found in [13]. In this setting the sensor illuminates a target at distance R_1. The tag receives the radar signal from the target at distance R_2. After modulation and amplification the signal is retransmitted and reflected once more at the target. The direct path between sensor and tag is possible in theory, but in practice it is subject to very high attenuation not only due to the free-space loss but also due to the limited gain of the antenna elements for signals at the edge of the usable field of view, which is the case here. The sensor node receives signals from the target directly (·····) and via the bistatic path including the tag (- - -). This makes it possible to receive signals transmitted at the tag location in the distance d_T from the sensor, but coming from the sensor originally. The modulation within the tag enables later differentiation of monostatic and bistatic responses. By doing so, the network yields the monostatic and bistatic ranges R_1 and R_2 of the target as well as the radial velocities v_1 and v_2. In principle, the concept can be scaled to a very large amount of tags. The limiting factor regarding the number of usable

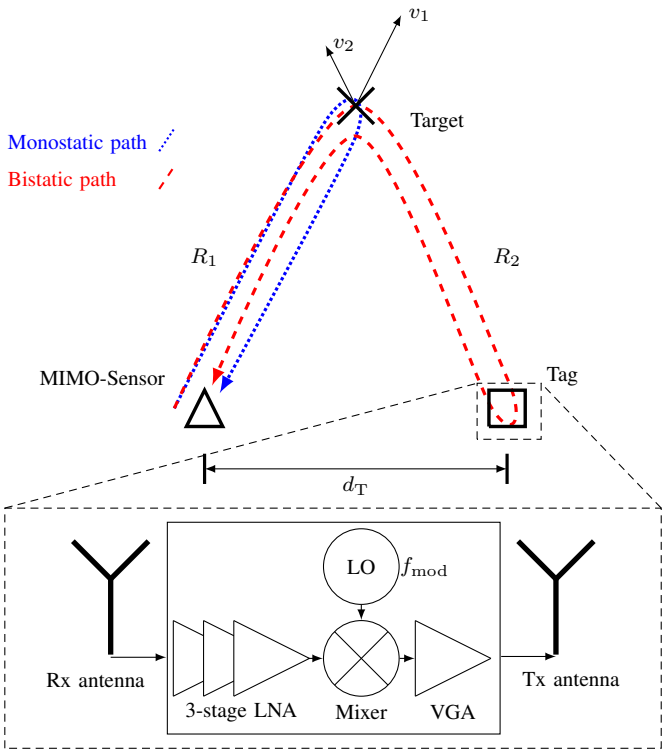

Fig. 1. Network consisting of one sensor and one tag in a single target scenario. The distance from sensor and tag to the target is given as R_1 and R_2 respectively. The distance between sensor and tag is d_T. The important parts of the tag are the low noise amplifier (LNA), the mixer with external local oscillator (LO) input and the variable gain amplifier (VGA).

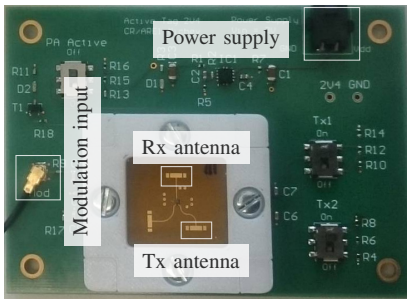

Fig. 2. Detailed view of the used repeater element as described in [13]. The essential components are highlighted.

tags is the available baseband bandwidth, which has to be divided to share it among all tags in the scene. The frequency of any of the modulated tag signals should not exceed the baseband bandwidth of the sensor. To illustrate the concept of the network, a scenario with one tag is assumed. The link between the baseband bandwidth and the tag modulation will become apparent in Section V, where simulations are presented.

In the following the MIMO configuration of the network is explained. Fig. 3 shows the MIMO virtual antenna array of the network including the tag. The transmit and receive antennas of the sensor span a regular MIMO virtual array (**I** in Fig. 3). The tag antenna represents an additional transmit antenna and yields another MIMO virtual array (**II** in Fig. 3). This additional transmit signal at the tag stems from the different

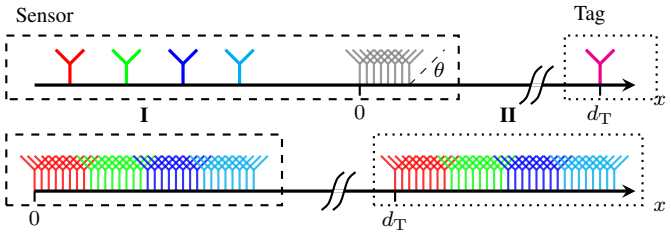

Fig. 3. Physical antenna positions (top) and virtual array positions (bottom) of sensor and tag Rx elements, shown for a 4-Tx, 8-Rx sensor array. Transmit antennas drawn in color, receiver antennas drawn in gray.

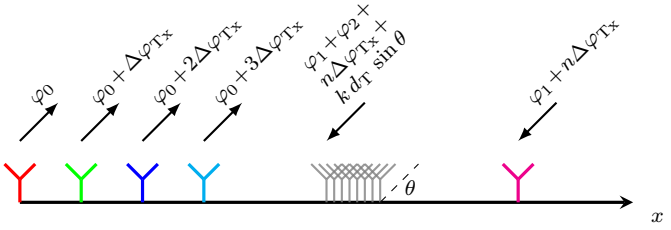

Fig. 4. Visualization of the phase values at the antenna elements in the MIMO system of Fig. 3. φ_0, φ_1 and φ_2 are arbitrary phases, n is the transmitter number ranging from 1 to N_{Tx}, and θ is the inclination angle of the target relative to the sensor.

transmit antennas of the sensor and depends on the target position. To process the monostatic and bistatic response jointly, a detailed look at the phase values in the system is necessary. The phase progression is visualized in Fig. 4, where the phase values at discrete points in the system of Fig. 1 are depicted. For the sake of simplicity, a uniform linear transmit array is assumed. φ_0 is a static offset phase, which is of no interest in this case. φ_1 is the change in phase for traveling the bistatic path from the first transmit antenna to the tag. φ_2 is the change of phase for traveling the bistatic path from the tag antenna to the first receiver. The term $n\,\Delta\varphi_{\mathrm{TX}}$ indicates the phase progression between the nth transmit antenna element relative to the first transmit antenna. The term $k\,d_{\mathrm{T}}\sin\theta$ contains the phase progression between sensor and tag for a target at angle θ, where k is the wavenumber and d_{T} is the distance between first receive antenna and tag antenna. To be able to treat the tag antenna as additional transmit antenna, the phase offset φ_1 has to be compensated. This phase correction is explained in detail in Section IV.

III. Signal Model

A. Classic FMCW/Chirp sequence

The classic FMCW radar signal processing according to [16] assumes a target at range R_1, velocity v_1, and angle θ_1. The radar sensor with center frequency f_c, ramp duration T and bandwidth B outputs a ramp with frequency

$$f_{\mathrm{T}}(t) = f_{\mathrm{c}} + \frac{B}{T}t\,. \tag{1}$$

The phase of the signal can be acquired by integration of the instantaneous angular frequency according to

$$\varphi(t) = 2\pi \int_{-T/2}^{t} f_{\mathrm{T}}(t)\;\mathrm{d}t + \phi_{\mathrm{PN}}(t)\,. \tag{2}$$

The signal travels from the sensor to the target and back within the time $\tau = 2(R_1 + v_1 t)$. The additive term $\phi_{\mathrm{PN}}(t)$ denotes the phase noise component of the transmitter. The phase of the down-converted received signal is given by

$$\begin{aligned}\Delta\varphi(t) &= \varphi(t) - \varphi(t-\tau)\\ &= 2\pi\left(f_c\tau + \frac{B}{T}t\tau - \frac{B}{2T}\tau^2\right)\\ &\quad + \phi_{\mathrm{PN}}(t) - \phi_{\mathrm{PN}}(t-\tau)\,.\end{aligned} \tag{3}$$

According to [17], the phase noise correlates at the receiver, if the received signal gets down-converted with the originally transmitted signal and if τ is small, which is assumed to be true. This yields the complex discrete phase of the baseband signal for every sample n and chirp l received as

$$s[n,l] = \exp\left(\mathrm{j}\,2\pi\left[\frac{2f_cR(l)}{c} + \left(\frac{2f_cv}{c} + \frac{2BR(l)}{Tc}\right)T_{\mathrm{A}}n\right]\right), \tag{4}$$

which is sampled with the frequency $1/T_{\mathrm{A}}$. The inter-chirp difference in the target position is considered by the chirp-dependent range $R(l)$, which is given as $R(l) = R + v\,T_{\mathrm{rep}}\,l$, where T_{rep} is the chirp repetition time. For a more detailed derivation, see [16].

B. FMCW/Chirp Sequence with Tag

By considering the tag element in the system, the formulas introduced above change and have to be adapted. The multistatic arrangement leads to four measurands, namely the distance between sensor and target R_1, target and tag R_2, the radial velocity seen from sensor v_1, and the radial velocity seen from tag v_2. Additionally, the tag modulates the incoming signal with modulation frequency f_{mod}. Moreover, instead of the signal runtime τ, the signal now travels two paths with delays $\tau_1 = (R_1 + v_1 t)/c$ and $\tau_2 = (R_2 + v_2 t)/c$. The receiver phase at the sensor node becomes

$$\begin{aligned}\Delta\varphi(t) &= \varphi(t) - \varphi(t-\tau)\\ &= \varphi(t) - \varphi(t-\tau)\Big|_{-\frac{T}{2}}^{-\frac{T}{2}+\frac{\tau_1+\tau_2}{2}} - \varphi(t-\tau)\Big|_{-\frac{T}{2}+\frac{\tau_1+\tau_2}{2}}^{t-\frac{\tau_1+\tau_2}{2}}\\ &= 2\pi\int_{-\frac{T}{2}}^{-\frac{T}{2}+\frac{\tau_1+\tau_2}{2}} f_{\mathrm{T}}(t)\,\mathrm{d}t - 2\pi\int_{-\frac{T}{2}+\frac{\tau_1+\tau_2}{2}}^{t-(\tau_1+\tau_2)/2} f_{\mathrm{T}}(t)\,\mathrm{d}t\,.\end{aligned} \tag{5}$$

After some simplifications this term becomes

$$\begin{aligned}\Delta\varphi(t) = &\left[(v_1+v_2)\frac{2\,f_c}{c} + (R_1+R_2)\frac{2\,B}{T\,c}\right]t\\ &+ \left[\frac{2\,R_1\,f_c}{c} + \frac{2\,R_2\,f_c}{c}\right].\end{aligned} \tag{6}$$

This is the phase of the received signal via the bistatic path without tag modulation. In the next step, the modulation of

the tag with frequency f_{mod} is considered. This leads to an extended phase term of

$$\Delta\varphi_{\mathrm{tag}}(t) = \Delta\varphi(t) + \left[-f_{\mathrm{mod}} + (v_1+v_2)\frac{3\,f_{\mathrm{mod}}}{c}\right] t + (R_1+R_2)\frac{3\,f_{\mathrm{mod}}}{c} - T\frac{f_{\mathrm{mod}}}{2}\,. \tag{7}$$

The complete derivation can be found in the Appendix.

Besides the terms occurring in (4), an additional phase term from the non-coherent modulation signal of the tag is present. The phase of the modulation signal is not set to zero at the beginning of each new ramp, as this signal is not coupled or triggered with the main sensor. Therefore, the phase difference between two consecutive ramps needs to be considered. Between each ramp, the phase of the modulation signal changes by

$$\varphi_{\mathrm{mod}} = 2\pi \int_{t_0}^{t_0+T_{\mathrm{rep}}} f_{\mathrm{mod}}\ \mathrm{d}t = 2\pi f_{\mathrm{mod}}\, T_{\mathrm{rep}}\,. \tag{8}$$

This results in an additional shift of the target response in the velocity domain of the Range-velocity-plot (R-v-plot). The modulation frequency also shifts the target response in the range domain of the R-v-plot, which helps to distinguish the monostatic from the bistatic response. The bistatic target peaks shifted by the tag modulation are beyond the range of interest of the monostatic response. Therefore the monostatic and bistatic target peaks can be clearly separated in the R-v domain. It needs to be ensured, however, that the intermediate frequency bandwidth of the sensor is large enough to not only cover the monostatic responses, but also the bistatic modulated responses. In practice this should not pose a problem, as the modulation frequency is typically at most a few MHz.

The phase of the received signal can then be processed by chirp sequence processing, which leads to a 2D-matrix with the entries according to

$$S^{\mathrm{RV}}[k,m] = \sum_{l=0}^{N_{\mathrm{c}}-1}\sum_{n=0}^{N_{\mathrm{s}}-1} s[n,l]\mathrm{e}^{-\mathrm{j}2\pi\left(\frac{kn}{N_{\mathrm{s}}}+\frac{ml}{N_{\mathrm{c}}}\right)}\,, \tag{9}$$

where k is the discrete range index, m the discrete Doppler index, N_{s} the number of samples, and N_{c} the number of chirps.

For a linear antenna array and a single target at angle θ the phase values are given as

$$S^{\mathrm{RV}}_{\substack{\mathrm{t,r}\\ t\in\{1,\dots,N_{\mathrm{Tx}}\}\\ r\in\{1,\dots,N_{\mathrm{Rx}}\}}}[k,m] = S^{\mathrm{RV}}[k,m]\,\mathrm{e}^{-\mathrm{j}(2\pi/\lambda)[(t-1)d_{\mathrm{Tx}}+rd_{\mathrm{Rx}}]\sin(\theta)}\,, \tag{10}$$

where d_{Tx} is the transmitter spacing, d_{Rx} the receiver spacing and θ the angle of arrival of the target.

The 2D-DFT processed signals for each transmitter-receiver antenna pair can be further processed to yield the angular spectrum as

$$S^{\mathrm{RVA}}_{\substack{\mathrm{t}\\ t\in\{1,\dots,N_{\mathrm{Tx}}\}}}[u,k,m] = \sum_{n=0}^{N_{\mathrm{Rx}}-1} S^{\mathrm{RV}}_{t,n}[k,m]\,\mathrm{e}^{-\mathrm{j}\frac{2\pi}{N_{\mathrm{Rx}}}un}\,, \tag{11}$$

where u is the discrete angular index.

IV. DoA Estimation with Compressed Sensing Reconstruction

The signals from the sensor and the tag are received simultaneously at the receive antennas of the sensor. It is assumed that all impinging signals are received at the same angle from a plane wavefront. In the following the steps necessary for a joint evaluation of the monostatic and bistatic phases are explained. For the sake of simplicity, only a single transmitter is considered here, as well as in the simulations and measurement evaluations involving the tag. However, the theory can be extended to the MIMO case accordingly.

A. Preprocessing

It is possible to do angle estimation with both the tag and the sensor responses separately or with both of them combined in a sparse array. In the latter case the resulting signal vector is very sparse and the need for a reconstruction algorithm arises. The key observation is that the virtual aperture of the MIMO sensor occurs at the location of the tag, which yields a total virtual aperture as given in Fig. 3. This comes from the fact that the tag can be considered as an additional Tx-antenna, whose transmit phase is a function of the target angle. To be able to successfully process the sparse signal, the distance between the tag and the sensor position has to be estimated. If the gap between the sensor and the tag is d_{T}, the distance in multiples of $\lambda/2$ is given as $N_{\mathrm{gap}} = d_{\mathrm{T}}/(\lambda/2)$. The receive antennas are spaced $\lambda/2$ apart, so the distance between sensor reference antenna position and tag antenna position is conveniently given in multiples of $\lambda/2$. Before the two vectors of monostatic and bistatic phases can be jointly processed, they have to be linked together. The monostatic received phases are given as

$$\Psi_{\mathrm{m}} = \left[\mathrm{e}^{-\mathrm{j}\varphi_{\mathrm{m},1}}, \mathrm{e}^{-\mathrm{j}\varphi_{\mathrm{m},2}}, \dots, \mathrm{e}^{-\mathrm{j}\varphi_{\mathrm{m},N_{\mathrm{Rx}}}}\right]\,, \tag{12}$$

and the bistatic received phases as

$$\Psi_{\mathrm{b}} = \left[\mathrm{e}^{-\mathrm{j}\varphi_{\mathrm{b},1}}, \mathrm{e}^{-\mathrm{j}\varphi_{\mathrm{b},1}}, \dots, \mathrm{e}^{-\mathrm{j}\varphi_{\mathrm{b},N_{\mathrm{Rx}}}}\right]\,. \tag{13}$$

To jointly process the two vectors of phase differences, the bistatic phase values have to be linked to the monostatic ones with

$$\tilde{\Psi}_{\mathrm{bi}} = \Psi_{\mathrm{bi}}/\Psi_{\mathrm{bi}}[1]\Psi_{\mathrm{mono}}[N_{\mathrm{Rx}}]\mathrm{e}^{-\mathrm{j}\Delta\varphi_{\mathrm{Rx}}N_{\mathrm{gap}}}\,. \tag{14}$$

The division term $\Psi_{\mathrm{bi}}[1]$ normalizes the phases Ψ_{bi} received from the tag to the first received bistatic phase value. The multiplication term $\Psi_{\mathrm{mono}}[N_{\mathrm{Rx}}]$ includes the phase difference from the first to the last monostatic receive phase. The exponential term $\mathrm{e}^{-\mathrm{j}\Delta\varphi_{\mathrm{Rx}}N_{\mathrm{gap}}}$ adds the phase difference from the last monostatic receive element to the tag antenna, where $\Delta\varphi_{\mathrm{Rx}}$ represents the phase difference between two monostatic Rx channels. To improve accuracy, the mean value between all monostatic phase differences is taken for $\Delta\varphi_{\mathrm{Rx}}$. With the compensated vector $\tilde{\Psi}_{\mathrm{bi}}$, it is possible to jointly process the sensor and tag phase values with N_{gap} zero elements in between. This results in one large, very sparse vector, as $N_{\mathrm{gap}} \gg N_{\mathrm{Rx}}$. The sparse vector consists of two sets of phase values, which can be interpreted as two rectangular blocks within the total array. The resulting sinc functions of these rectangular blocks after the Fourier transform produce a huge

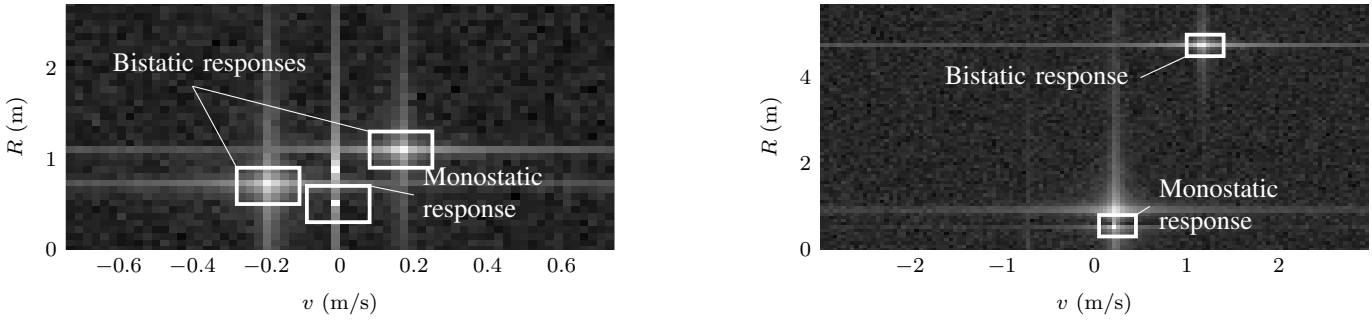

(a) (b)

Fig. 5. R-v-plot of a single target (simulation). Monostatic target peak (from sensor) and bistatic target peak (from tag with modulation) are highlighted. (a) Static target in 45 cm distance, $f_{\mathrm{mod}} = 10\,\mathrm{kHz}$. (b) Moving target in 45 cm distance with $v_x = 0.5\,\mathrm{m/s}$, $f_{\mathrm{mod}} = 201.7\,\mathrm{kHz}$.

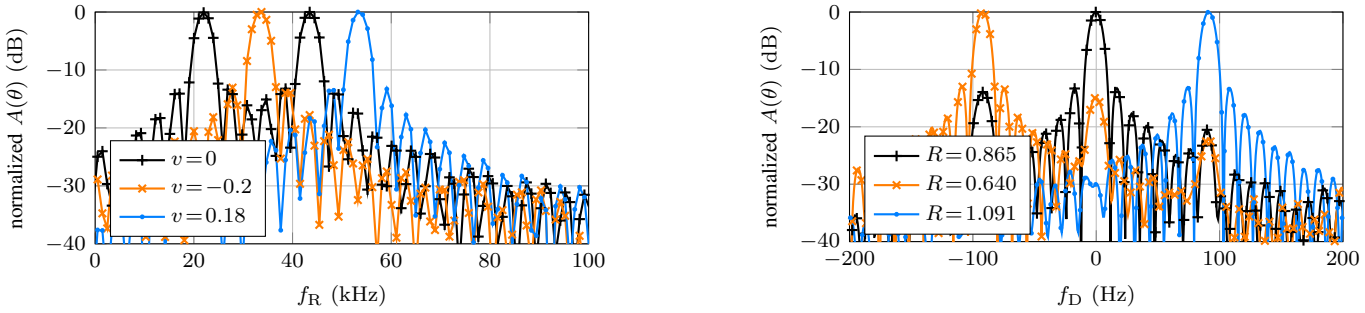

(a) (b)

Fig. 6. (a) Range-DFT and (b) Doppler-DFT over bins of interest (simulation). The modulation frequency is $f_{\mathrm{mod}} = 10\,\mathrm{kHz}$ and the static target is placed in 40 cm distance. No windowing is applied before the DFT to avoid peak broadening.

number of peaks. To get the true target angle, a compressed sensing (CS) reconstruction is carried out.

B. Compressed Sensing Reconstruction

In the measurement evaluation the signal is reconstructed using the iterative hard thresholding (IHT) algorithm [18], which is adapted to the problem at hand. IHT belongs to the CS algorithms and is similar to the more advanced iterative method for adaptive thresholding (IMAT) algorithm [19], where the exact sparsity of the signal is not required. For a general introduction to CS the reader is referred to [20], [21], [22]. For an overview of CS in radar, see [23]. The IHT algorithm is selected as a straightforward tool to verify the proposed system concept. The algorithm iteratively tries to minimize the residual signal energy. The residual is calculated with the exclusion of phase information coming from the non-filled antenna positions. In each iteration a signal proxy $\tilde{\mathbf{x}}$ is calculated, which is based on the current best guess for the spectrum and the residual. After generation of the signal proxy, a new guess for $\mathbf{x}$ is calculated as $\hat{\mathbf{x}}$, where the spectral components that lie under the selected threshold are set to zero. The chosen threshold is dependent on the assumed number of targets. In the subsequent simulations and measurements, the threshold is set to the highest peak in the spectrum. If a multi-target setting is evaluated, the algorithm is run multiple times to extract multiple peaks. In that case the input for consecutive runs of the algorithm is corrected with the residual of the previous run.

TABLE I
TABLE OF SIMULATION PARAMETERS

Parameter	Target with $v = 0$	Target with $v \neq 0$
f_c	77 GHz	77 GHz
B	2 GHz	2 GHz
T_c	256 µs	256 µs
T_{rep}	$4\,(T_c + 72\,\mu\mathrm{s})$	$T_c + 72\,\mu\mathrm{s}$
f_s	1 MHz	4 MHz
$N_{\mathrm{Tx}} \times N_{\mathrm{Rx}}$	4×8	1×4
N_{chirp}	64	128

V. Simulations

In this section, simulation results are presented based on the mathematical framework derived earlier. A static and a moving target are evaluated with the selected radar parameters given in Table I. Path losses are not considered in the simulations. A single cylindrical target is positioned 40 cm in front of a repeater tag. Next to the repeater tag a 1-Tx, 4-Rx SIMO sensor is placed. The sensor and the tag are separated by a distance of 20 cm. This results in a target distance of 45 cm. The target is mounted on a linear rail which, when operated, moves the target parallel to sensor and tag at a velocity of 0.5 m/s.

A. Static Target

First, a scenario with a static target at 45 cm distance to the sensor is simulated. The modulation frequency at the tag is set to 10 kHz and the spacing between sensor and tag to 20 cm.

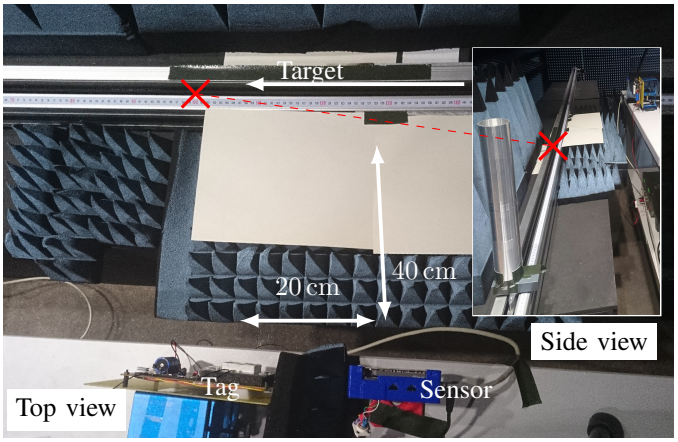

Fig. 7. Measurement setup with a 1-Tx, 4-Rx SIMO sensor, a tag and a cylinder target. The target is 40 cm apart from the tag, the tag 20 cm apart from the sensor. When moving, the target has a velocity of 0.5 m/s in the indicated direction. The red cross marks the measured position.

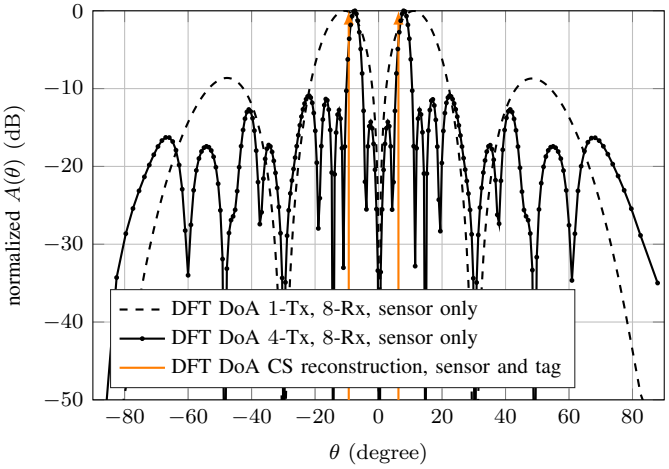

Fig. 8. DoA estimation (simulation), $f_{\mathrm{mod}} = 10\,\mathrm{kHz}$, two targets in 60 cm distance at angles $\pm 7.6°$. The distance between the last receive antenna of the sensor and the tag is assumed to be $95\lambda/2$ corresponding to $d_{\mathrm{T}} = 0.2\,\mathrm{m}$ measured from the first receive antenna to the tag.

In Fig. 5 (a) the simulation result after the 2D-DFT is presented. The double-sideband BPSK modulator of the tag generates two target peaks that are shifted in range and velocity, which are marked as "bistatic responses". In Fig. 5 (b) only the target peak for the upper sideband is visible, the lower peak is shifted to negative frequencies and therefore not within the plot range. At approximately twice the distance of the monostatic target peak, another bistatic peak is visible in Fig. 5 (a) and Fig. 5 (b). This is the bistatic target peak via the tag without tag modulation. This target response is therefore not shifted. The shift in range corresponds to the given modulation frequency of 10 kHz and can be calculated as

$$R_{\mathrm{shift}} = \frac{f_{\mathrm{mod}}\, T_{\mathrm{c}}\, c}{2\, B}\,. \tag{15}$$

In the above introduced scenario with $f_{\mathrm{mod}} = 10\,\mathrm{kHz}$ this would correspond to a range offset of 19.2 cm. A plot of the monostatic and bistatic target frequencies including f_{mod} can be seen in Fig. 6. The velocity shift corresponds to the given ramp repetition interval and the modulation frequency and can be calculated as

$$f_{\mathrm{D,s}} = \begin{cases} \mathrm{mod}\left(f_{\mathrm{mod}}, \frac{1}{2\,T_{\mathrm{r}}}\right) & \text{if } \mathrm{mod}\left(\left\lfloor \frac{f_{\mathrm{mod}}}{\frac{1}{2\,T_{\mathrm{r}}}} \right\rfloor, 2\right) = 0 \\ \mathrm{mod}\left(f_{\mathrm{mod}}, \frac{1}{2\,T_{\mathrm{r}}}\right) - \frac{1}{2\,T_{\mathrm{r}}} & \text{else} \end{cases} \tag{16}$$

which results in a velocity offset of

$$v_{\mathrm{shift}} = \frac{f_{\mathrm{D,s}}\, c}{2\, f_{\mathrm{c}}}\,.$$

For a modulation frequency of 10 kHz, this results in a Doppler frequency offset of $f_{\mathrm{D,s}} = 91.46\,\mathrm{Hz}$ and an offset velocity of $v_{\mathrm{shift}} = 0.18\,\mathrm{m/s}$, which can also be seen in Fig. 6. The calculated range and Doppler shifts of the static target match well with the values from the simulation extracted from Fig. 6.

B. Moving Target

In the next step, a moving target is simulated. The target is moving on a linear rail with a velocity component of $v_x = 0.5\,\mathrm{m/s}$. The arrangement of sensor, tag, and linear rail is shown in Fig. 7. For the simulation the target is located in front of the tag and the modulation frequency is set to 201.7 kHz to achieve an offset in the velocity domain of the R-v-plot of approximately 1 m/s.

The resulting R-v-plot in Fig. 5 (b) is similar to the static target case, except that the target now has an additional velocity component besides the shift coming from the modulation frequency. The radial velocity seen by the sensor is $v_{\mathrm{r,sensor}} = v_x \cos(\mathrm{atan}(0.4/0.2)) = 0.22\,\mathrm{m/s}$. The radial velocity seen by the tag is zero, as the target is directly in front of the tag with only a lateral velocity component. Therefore, including the velocity shift of $v_{\mathrm{shift}} \approx 1\,\mathrm{m/s}$, the modulated target peak is expected at 1.22 m/s. The bistatic target peak in Fig. 5 (b) matches with the calculated position.

C. Angle Estimation

Eventually, the angle estimation capabilities are simulated. A two target scenario is selected, in which the targets are placed 60 cm in front of the sensor at the angles $\pm 7.6°$. The tag is again placed 20 cm next to the sensor. In Fig. 8 the resulting angular spectrum is plotted for a 1-Tx, 8-Rx single-input-multiple-output (SIMO) array, a 4-Tx, 8-Rx MIMO array and a 1-Tx, 8-Rx SIMO array including tag. In the last case, the CS algorithm was run twice to produce two target peaks, as described in Section IV. The estimated spectrum with tag response results in much narrower peaks as compared to the sensor-only cases and matches the real target positions well.

VI. Measurements

In the following the theoretical considerations are validated by measurements. The radar sensor parameters are the same as for the simulations according to Table I. At first, measurements were made to confirm the simulations in regard to the bistatic range and velocity. This was done both for a static and a moving cylinder target. Subsequently, the angle estimation

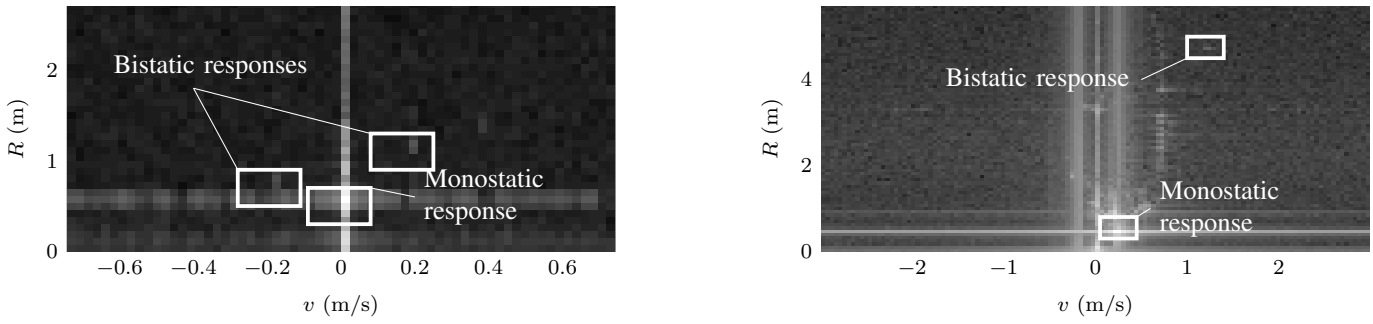

(a) (b)

Fig. 9. R-v-plot measurement with Radar sensor and tag (see Table I). Target is on linear rail in front of sensor and tag. (a) Stationary target in 45 cm distance, $f_{\mathrm{mod}} = 10\,\mathrm{kHz}$. (b) Moving target in 45 cm distance with $v_x = 0.5\,\mathrm{m/s}$.

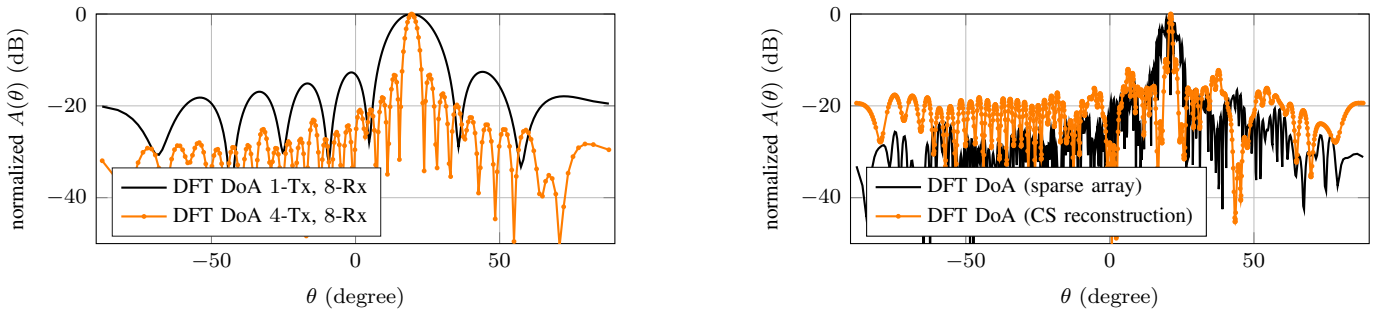

(a) (b)

Fig. 10. DoA estimation of the single target. Comparison between (a) sensor only evaluation with 1-Tx, 8-Rx SIMO and (b) 4-Tx, 8-Rx MIMO and joint evaluation of sensor (with 1-Tx, 8-Rx SIMO) and tag with compressed sensing reconstruction.

capabilities of the system are evaluated for a single target as well as for two closely-spaced static targets.

A. Range-velocity Evaluation of a Static Target

The measurement setup for a static target is depicted in Fig. 7. The target is placed on a table at a distance of approximately 45 cm from the sensor. The resulting R-v-plot in Fig. 9 (a) clearly shows the modulation peaks from the tag as expected from the simulated R-v-plot of Fig. 5 (a). The extracted monostatic target is at $(0.55\,\mathrm{m}, 0\,\mathrm{m/s})$, the bistatic target is at $(1.18\,\mathrm{m}, 0.2\,\mathrm{m/s})$.

B. Range-velocity Evaluation of a Target in Motion

Next, the R-v evaluation of a moving target is presented. The radar parameters and settings are given in Table I. The measurement setup is depicted in Fig. 7. The monostatic target peak is at $(0.45\,\mathrm{m}, 0.21\,\mathrm{m/s})$ and the modulated target peak is at $(4.75\,\mathrm{m}, 1.25\,\mathrm{m/s})$ within the R-v-plot of Fig. 9 (b). The measured velocities agree with the velocities expected from the simulation. This means, that also for targets with radial velocity components, the earlier derived mathematical framework holds true. Therefore R_1, R_2, v_1, and v_2 can be measured via the proposed approach.

C. Angle Estimation

1) Single target: For the angle estimation of a single target, the measurement data from the setup in Fig. 7 is considered. The target is placed at an angle of approximately 20° and 45 cm distance to the sensor. The phases of the monostatic and bistatic R-v bins of Fig. 9 (a) for all virtual channels are evaluated to estimate the direction of arrival of the targets. From Fig. 10 the performance between using only the sensor and the joint approach with sensor and tag can directly be compared. With a 1-Tx, 8-Rx SIMO system the peak in the angular domain is quite broad, which will narrow if the system is evaluated as 4-Tx, 8-Rx MIMO system. The joint approach with sensor and tag yields an angle detection performance comparable to the 4-Tx, 8-Rx MIMO system but relying only on the 1-Tx, 8-Rx phase data of the sensor plus the response received from the tag. This proves that by deploying the tag in the MIMO system a performance increase in the angle estimation can be achieved.

2) Two closely spaced targets: The last setup, as seen from Fig. 11, consists of two targets spaced 17 cm apart at a distance of 60 cm to the sensor node. As a reference, the monostatic target responses are again evaluated for a 1-Tx, 8-Rx SIMO and a 4-Tx, 8-Rx MIMO antenna system. The reference measurement and the measurement including the tag response are shown in Fig. 12. For the monostatic evaluation the two cylinder targets can not be discerned in case of the 1-Tx, 8-Rx SIMO antenna array. Only after evaluation of the complete 4-Tx, 8-Rx MIMO virtual array, the two targets are separable. In contrast, by using only the 1-Tx, 8-Rx phase data with additional tag, the two targets can be extracted, which is the bottom plot of Fig. 12. The extracted target peaks using

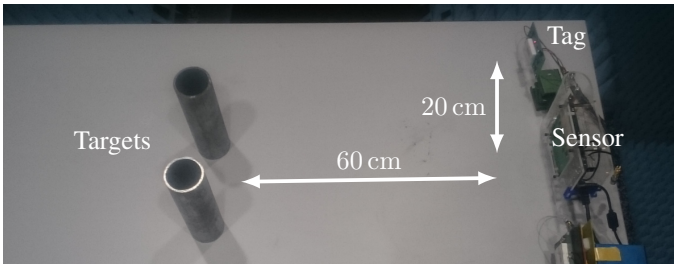

Fig. 11. Measurement setup with a 4-Tx, 8-Rx MIMO sensor, the tag and two cylinder targets. The targets are placed at the angles $\pm 7.5^\circ$ with respect to the sensor.

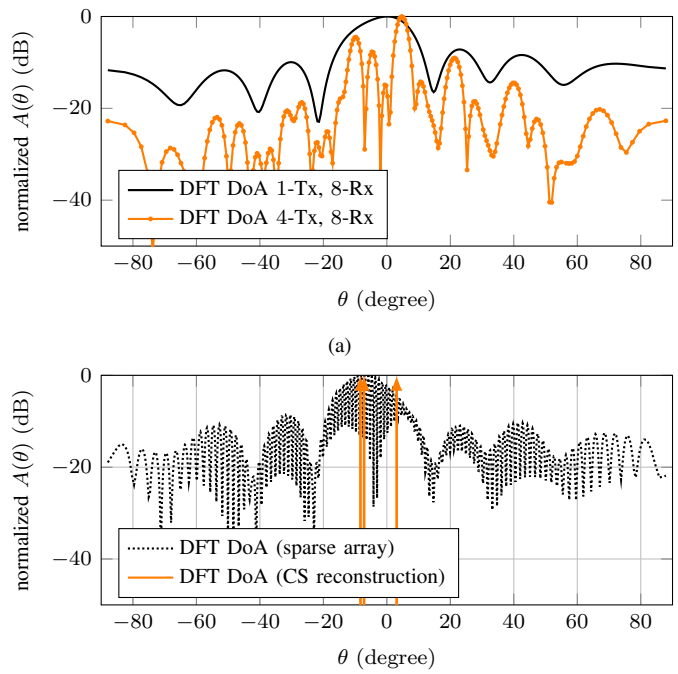

Fig. 12. DoA estimation of the two closely spaced targets in Fig. 11. Comparison between (a) sensor only evaluation with 1-Tx, 8-Rx SIMO and 4-Tx, 8-Rx MIMO and (b) joint evaluation of sensor (with 1-Tx, 8-Rx SIMO) and tag with compressed sensing reconstruction.

the tag match well with the reference evaluation including only the monostatic response.

VII. Conclusion

The introduction of a new transmitter-receiver element ("repeater tag") in a conventional chirp sequence radar system was evaluated. By utilizing the tag it was possible to show that bistatic radar measurements could successfully be acquired without the need of coherently coupled sensor nodes. The tag acts as a coherent station relative to a transmitting master sensor, but only needs a power supply and a modulation input. This makes the tag ideal for network distribution within a more complex radar framework, as it is simple to integrate and easy to operate. The measurements that were carried out showed the capability of the new MIMO network. The bistatic tag response was jointly processed with the monostatic response to form a radar network, in which the performance benefits of the network in comparison to a single sensor could be shown. With the network it is possible to measure the monostatic range R_1 and velocity v_1 as well as the bistatic range R_2 and velocity v_2 of the targets. The angle of arrival θ can be measured monostatically and jointly using the tag to improve the resolution. In summary, it was possible to show that a bistatic radar network can be built consisting only of one (MIMO)-radar sensor and one or more simple repeater tags. Compared to a single sensor setup, the measurements show that the tag network leads to an improved radar performance.

Appendix

In the following, the receive phase $\Delta\varphi_{\mathrm{RX}}(t)$ for a bistatic received signal is calculated.

$$
\begin{aligned}
\Delta\varphi_{\mathrm{RX}}(t) &= \varphi(t)-\varphi(t-\tau) \\
&= \varphi(t)-\varphi(t-\tau)\Big|_{-T/2}^{-T/2+\frac{\tau_1+\tau_2}{2}} - \varphi(t-\tau)\Big|_{-\frac{T}{2}+\frac{\tau_1+\tau_2}{2}}^{t-\frac{\tau_1+\tau_2}{2}} \\
&= 2\pi \int_{-\frac{T}{2}}^{-\frac{T}{2}+\frac{\tau_1+\tau_2}{2}} f_{\mathrm{T}}(t)\,dt - 2\pi \int_{-\frac{T}{2}+\frac{\tau_1+\tau_2}{2}}^{t-(\tau_1+\tau_2)/2} f_{\mathrm{T}}(t)\,dt \\
\Delta\varphi_{\mathrm{RX}}(t) &= \tfrac{(T+2t)\,(2Bt+4Tf_c-BT)}{8T} \\
&-\tfrac{1}{8Tc^2}\,(6R_1+6R_2-Tc-2ct+6tv_1+6tv_2) \\
&\times (2BR_1+2BR_2+BTc-2Bct-4Tcf_c+2Btv_1+2Btv_2) \\
&-\tfrac{1}{2Tc^2}\,(R_1+R_2+tv_1+tv_2) \\
&\times (BR_1+BR_2-BTc+2Tcf_c+Btv_1+Btv_2)
\end{aligned}
$$

All terms with c^2 in the denominator or t^2 in the nominator can be neglected, leading to

$$
\begin{aligned}
\Delta\varphi_{\mathrm{RX}}(t) &= \tfrac{2R_1f_c}{c}+\tfrac{2R_2f_c}{c}+\tfrac{2f_ctv_1}{c}+\tfrac{2f_ctv_2}{c}+\tfrac{2BR_1t}{Tc}+\tfrac{2BR_2t}{Tc} \\
&= \left[(v_1+v_2)\cdot\tfrac{2f_c}{c}+(R_1+R_2)\cdot\tfrac{2B}{Tc}\right]\cdot t+\left(\tfrac{2R_1f_c}{c}+\tfrac{2R_2f_c}{c}\right).
\end{aligned}
$$

The same can be derived including an additional modulation f_{mod} by the tag

$$
\begin{aligned}
\Delta\varphi_{\mathrm{RX}}(t) &= \tfrac{2R_1f_c}{c}+\tfrac{2R_2f_c}{c}-f_{\mathrm{mod}}\,t-\tfrac{Tf_{\mathrm{mod}}}{2}+\tfrac{3R_1f_{\mathrm{mod}}}{c}+\tfrac{3R_2f_{\mathrm{mod}}}{c} \\
&+\tfrac{2f_ctv_1}{c}+\tfrac{2f_ctv_2}{c}+\tfrac{3f_{\mathrm{mod}}tv_1}{c}+\tfrac{3f_{\mathrm{mod}}tv_2}{c}+\tfrac{2BR_1t}{Tc}+\tfrac{2BR_2t}{Tc} \\
&= \left[(v_1+v_2)\tfrac{2f_c}{c}+(R_1+R_2)\tfrac{2B}{Tc}-f_{\mathrm{mod}}+(v_1+v_2)\cdot\tfrac{3f_{\mathrm{mod}}}{c}\right]t \\
&+\left(\tfrac{2R_1f_c}{c}+\tfrac{2R_2f_c}{c}+(R_1+R_2)\cdot\tfrac{3f_{\mathrm{mod}}}{c}-T.\tfrac{f_{\mathrm{mod}}}{2}\right)
\end{aligned}
$$

References

[1] R. Lachner, "Industrialization of mmWave SiGe technologies: Status, future requirements and challenges," in *IEEE 13th Topical Meeting on Silicon Monolithic Integrated Circuits in RF Systems*, Jan. 2013, pp. 105–107.

[2] C. M. Schmid, R. Feger, C. Pfeffer, and A. Stelzer, "Motion compensation and efficient array design for TDMA FMCW MIMO radar systems," in *6th Eur. Conf. on Antennas and Propagation (EUCAP)*. IEEE, 2012, pp. 1746–1750.

[3] Z. Peng and C. Li, "A Portable$K$-Band 3-D MIMO Radar With Nonuniformly Spaced Array for Short-Range Localization," *IEEE Trans. Microw. Theory Techn.*, vol. 66, no. 11, pp. 5075–5086, Nov. 2018.

[4] D. Bleh, M. Rösch, M. Kuri, A. Dyck, A. Tessmann, A. Leuther, S. Wagner, B. Weismann-Thaden, H. . Stulz, M. Zink, M. Rießle, R. Sommer, J. Wilcke, M. Schlechtweg, B. Yang, and O. Ambacher, "W -Band Time-Domain Multiplexing FMCW MIMO Radar for Far-Field 3-D Imaging," *IEEE Trans. Microw. Theory Techn.*, vol. 65, no. 9, pp. 3474–3484, Sep. 2017.

[5] R. Feger, C. Pfeffer, W. Scheiblhofer, C. M. Schmid, M. J. Lang, and A. Stelzer, "A 77-GHz Cooperative Radar System Based on Multi-Channel FMCW Stations for Local Positioning Applications," *IEEE Trans. Microw. Theory Techn.*, vol. 61, no. 1, pp. 676–684, Jan. 2013.

[6] A. Frischen, J. Hasch, and C. Waldschmidt, "Contour recognition with a cooperative distributed radar sensor network," in *IEEE MTT-S Int. Conf. on Microwaves for Intelligent Mobility (ICMIM)*, Apr. 2015, pp. 1–4.

[7] F. Folster, H. Rohling, and U. Lubbert, "An automotive radar network based on 77 GHz FMCW sensors," in *IEEE Int. Radar Conf.*, May 2005, pp. 871–876.

[8] A. Frischen, J. Hasch, and C. Waldschmidt, "A Cooperative MIMO Radar Network Using Highly Integrated FMCW Radar Sensors," *IEEE Trans. Microw. Theory Techn.*, vol. 65, no. 4, pp. 1355–1366, 2017.

[9] ——, "Performance degradation in cooperative radar sensor systems due to uncorrelated phase noise," in *11th Eur. Radar Conf. (EuRAD)*. IEEE, 2014, pp. 241–244.

[10] M. C. Budge and M. P. Burt, "Range correlation effects in radars," in *The Rec. of the IEEE Nat. Radar Conf.*, 1993, pp. 212–216.

[11] K. Siddiq, R. J. Watson, S. R. Pennock, P. Avery, R. Poulton, and B. Dakin-Norris, "Phase noise analysis in fmcw radar systems," in *Eur. Radar Conf. (EuRAD)*, Sep. 2015, pp. 501–504.

[12] S. A. Maas, *Nonlinear microwave and RF circuits*. Artech house, 2003.

[13] M. S. Dadash, J. Hasch, P. Chevalier, A. Cathelin, N. Cahoon, and S. P. Voinigescu, "Design of Low-Power Active Tags for Operation With 77–81-GHz FMCW Radar," *IEEE Trans. Microw. Theory Techn.*, vol. 65, no. 12, pp. 5377–5388, Dec. 2017.

[14] J. Li and P. Stoica, Eds., *MIMO Radar Signal Processing*. John Wiley & Sons, Inc., Oct. 2008.

[15] R. Feger, C. Wagner, S. Schuster, S. Scheiblhofer, H. Jager, and A. Stelzer, "A 77-GHz FMCW MIMO radar based on an SiGe single-chip transceiver," *Trans. Microw. Theory Techn.*, vol. 57, no. 5, pp. 1020–1035, 2009.

[16] V. Winkler, "Range Doppler detection for automotive FMCW radars," in *Eur. Microwave Conf.* IEEE, 2007, pp. 1445–1448.

[17] S. J. Goldman, *Phase noise analysis in radar systems using personal computers*. Wiley, 1989.

[18] T. Blumensath and M. E. Davies, "Iterative hard thresholding for compressed sensing," *Appl. and Computational Harmonic Analysis*, vol. 27, no. 3, pp. 265–274, 2009.

[19] M. Azghani and F. Marvasti, "Iterative methods for random sampling and compressed sensing recovery," in *10th Int. Conf. on Sampling Theory and Appl. (SAMPTA)*, 2013.

[20] E. J. Candès, "Compressive sampling," in *Proc. of the Int. Congr. of Mathematicians*, vol. 3. Madrid, Spain, 2006, pp. 1433–1452.

[21] E. J. Candès, J. Romberg, and T. Tao, "Robust uncertainty principles: exact signal reconstruction from highly incomplete frequency information," *IEEE Trans. Inf. Theory*, vol. 52, no. 2, pp. 489–509, Feb. 2006.

[22] E. J. Candès and T. Tao, "Near-Optimal Signal Recovery From Random Projections: Universal Encoding Strategies?" *IEEE Trans. Inf. Theory*, vol. 52, no. 12, pp. 5406–5425, Dec. 2006.

[23] M. A. Hadi, S. Alshebeili, K. Jamil, and F. E. A. El-Samie, "Compressive sensing applied to radar systems: an overview," *Signal, Image and Video Processing*, vol. 9, no. 1, pp. 25–39, Dec. 2015.

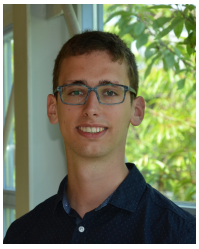

Benedikt Meinecke received the M. Sc. degree in electrical engineering with a focus on communication technology from the University of Ulm in 2017. He is currently pursuing the degree of Ph. D. in electrical engineering at the Institute of Microwave Engineering, Ulm University, Ulm, Germany.

His research interests include system concepts for multistatic coherent radar networks as well as the accompanying signal processing.

Maximilian Steiner received his master's degree (M. Sc.) in electrical engineering from the University of Ulm in 2015. He is currently pursuing the degree of Ph. D. in electrical engineering at the Institute of Microwave Engineering, Ulm University, Ulm, Germany.

His research interests include system concepts for radar sensor networks in automotive and robotic scenarios as well as the accompanying signal processing for cooperative radar-imaging, motion estimation, and localization.

Johannes Schlichenmaier received his Diploma degree in electrical engineering with a focus on microwave engineering from the Karlsruhe Institute of Technology (KIT), formerly the University of Karlsruhe, Karlsruhe, Germany in 2013. He is currently pursuing the degree of Ph. D. in electrical engineering at the Institute of Microwave Engineering, Ulm University, Ulm, Germany.

His research interests include advanced signal processing for cooperative radar networks in automotive scenarios, as well as detection and estimation of extended radar objects in dynamic traffic scenarios.

Jürgen Hasch (M'99–SM'13) received the Dipl. Ing. and Dr. Ing. degrees from the University of Stuttgart, Stuttgart, Germany, in 1996 and 2007, respectively. He is currently a Senior Expert on RF technology with Corporate Sector Research and Advance Engineering, Robert Bosch GmbH, Renningen, Germany. He has authored or co-authored over 40 scientific papers and holds over 20 patents. His current research interests include RF-based sensing technologies, integrated millimeter-wave sensors in the 60–240-GHz range, and novel modulation schemes. Dr. Hasch is a member of MTT TCC-27 and ITG-FA Mikrowellentechnik. He serves as a Reviewer for several journals and conferences.

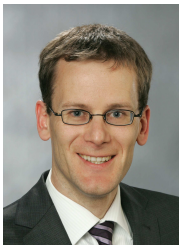

Christian Waldschmidt (S'01–M'05–SM'13) received the Dipl. Ing. (M. S. E. E.) and Dr.-Ing. (Ph. D. E. E.) degrees from the University of Karlsruhe, Karlsruhe, Germany, in 2001 and 2004, respectively. From 2001 to 2004, he was a Research Assistant with the Institut für Höchstfrequenztechnik and Elektronik, University of Karlsruhe. Since 2004, he has been with Robert Bosch GmbH in the business unit's Corporate Research and Chassis Systems. He was heading different research and development teams in microwave engineering, RF-sensing, and automotive radar. In 2013, he became a Full Professor with the Director of the Institute of Microwave Engineering, University Ulm, Ulm, Germany. He has authored or co-authored over 100 scientific publications and over 20 patents. His current research interests include radar and RF-sensing, millimeter-wave and submillimeter-wave engineering, antennas and antenna arrays, and RF and array signal processing. Dr. Waldschmidt is the Vice Chair of the IEEE MTT-27 Technical Committee (Wireless Enabled Automotive and Vehicular Applications), the Executive Committee Board member of the German MTT/AP Joint Chapter, and a member of the ITG Committee Microwave Engineering. In 2015, he served as the TPC Chair of the IEEE Microwave Theory and Techniques Society International Conference on Microwaves for Intelligent Mobility. He is a Reviewer for multiple IEEE Transactions and Letters.